Evaluation of Postharvest Senescence in Broccoli Via Hyperspectral Imaging

Xiaolei Guo[1, ¶], Yogesh Ahlawat[2, ¶], Alina Zare[1]*, Tie Liu[2]*

[1] University of Florida, Department of Electrical and Computer Engineering, Gainesville, Florida United States of America

[2] University of Florida, Horticultural Science Department, Gainesville, Florida, United States of America

* Corresponding author

Email: azare@ece.ufl.edu (AZ) and tieliu@ufl.edu (TL) ("AZ and TL are Joint Senior Authors")

¶ These authors contributed equally to this work

ABSTRACT

Fresh fruits and vegetables are invaluable for human health, but their quality deteriorates before reaching consumers due to ongoing biochemical processes and compositional changes. The current lack of any objective indices for defining "*freshness*" of fruits or vegetables limits our capacity to control product quality leading to food loss and waste. It has been hypothesized that certain proteins and compounds such as glucosinolates can be used as an indicator to monitor the freshness of vegetables and fruits. However, it is challenging to "visualize" the proteins and bioactive compounds during the senescence processes. In this work, we propose machine learning hyperspectral image analysis approaches for estimating glucosinolates levels to detect postharvest senescence in broccoli. Therefore, we set out the research to quantify glucosinolates as "freshness-indicators" which aid in the development of an innovative and accessible tool to precisely estimate the freshness of produce. Such a tool would allow for significant advancement in postharvest logistics and supporting the availability for high-quality and nutritious fresh produce.

Introduction

Broccoli (*Brassica oleracea* L. var. *italica*) is a nutritious vegetable that is well enriched in anti-cancerous chemical compounds like glucosinolates [1]. Broccoli is highly perishable and senesces quickly after harvest. Broccoli is usually harvested at a developing stage of

inflorescence therefore causes stress-induced senescence. The stress-induced senescence leads to faster chlorosis and increases in proteases resulting in the dismantling of chloroplast number and component [2]. Thus, during the postharvest storage and transportation, broccoli florets starts to turn yellow accompanied with a decrease in nutritional quality [1].

Senescence is a developmental process that can be tracked by monitoring physiological and biochemical changes in transcripts, proteins, and metabolites in broccoli. One particularly interesting class of phytochemicals are glucosinolates, given their importance not only for plant protection, but also for their dietary significance as chemo-preventative compounds that are found in edible plants, (i.e., cruciferous crops). However, the actual quality, storability and overall "freshness" of broccoli postharvest is quite uncertain unless the changes are visible to the human eye. Detecting any deteriorative physiological signs and symptoms before any irreversible damage occurs could allow for the development of freshness indicators, which can be used to identify the best postharvest handling, process and storage practices [3]. Therefore, sensitive indicators of potential deterioration are essential for extending optimal postharvest quality.

Prior work to detect symptoms of degradation in quality include using color measurements at an early postharvest stages [4]. Chlorophyll fluorescence and RGB (red, green, blue) color imagery analysis were used to measure the pigment change in broccoli using florescence and inverse red channel for color measurements [5]. However, objectively measuring the progressive loss of freshness after harvest has been a heretofore intractable problem in postharvest handling of fresh produce. Until now, determining freshness has been mostly based on external visual criteria like wilting, shriveling and color changes, which is laborious, time-consuming, and subjective [5].

The rapid advancement of optical sensors and imaging technologies has significantly impacted agriculture and brought about more automation [6]. Initially, imaging techniques used red-green-blue color systems for the identification of color change and defects in the food and agricultural products [7]. Since, multispectral fluorescence imaging has been used with maize, peas, soybean for measuring color change [8].

Hyperspectral Imaging (HSI) has also evolved over the years and is being explored as technique for nondestructive food analysis. HSI provides both spatial and spectral information about an object. HSI consists of many thousands of pixels in a two-dimensional array, with each pixel containing a spectrum corresponding to a specific region on the surface of the sample. These spectra vary according to unique material and chemical compositions. Interrogation of these spectra makes possible the development of mathematical models to estimate the chemical composition or functional class of a sample associated with each pixel. Results reported in several studies have indicated that hyperspectral imaging is able to predict a number of food components and quality parameters in a wide range of biological matrices [5]. Previous research has shown that HSI was used in a plethora of applications in agriculture and food industry to measure the textural changes including bruise, chilling injury, firmness [9,10,11], and biochemical detection such as moisture content, soluble solids content, acidity, and phenolics [12, 13,14], biosafety measurement in bacterial or fungal infection and fruit-fly infestation [15,16]. In addition, photosynthetic rate in mangroves was studied in relation to salinity stress using HSI technology [5]. More importantly, Hernandez et al. [17] reported that hyperspectral imaging can quantify the localization and total glucoraphanin in florets and stalks of broccoli. Moreover, the low instrument cost and fast-detecting properties of HSI have enabled the

development of powerful diagnostic tools for detecting, classifying, and visualizing quality and safety attributes of fresh produce.

This study was conducted to evaluate the potential significance of hyperspectral imaging as a tool to determine the freshness of broccoli during postharvest storage. Through High Performance Liquid Chromatography (HPLC) quantitation, we showed that there is a linear correlation between the total glucosinolates concentration and post-harvest senescence in broccoli. Moreover, we performed Real-Time Polymerase Chain Reaction (PCR) for expression studies on 13 enzymes are involved in the biochemical pathway producing glucosinolates. We believe that combination of HSI and glucosinolates analysis can define the freshness signature in postharvest broccoli.

Materials and methods

Tissue collection and Preparation

Freshly grown broccoli (cultivar, Emerald Crown) florets were manually harvested from local farms in Hastings, Florida to avoid any mechanical damage. All the broccoli florets were selected with the same shape and size in this study. The florets were then stored in either a cold room (4–5°C, darkness) for the cold treatment, or in a plant growth chamber at 25°C (RT) with 16 hours of light and 8 hours of dark. Four biological replicate of broccoli florets were used for the experimental sampling for tissue collections. Tissue samples were collected from the broccoli florets every other day during a twelve-day period. The samples were wrapped in aluminum foil,

immediately frozen in liquid nitrogen and then stored in -80°C for quantitative PCR and freeze-dried for HPLC.

Hyperspectral imaging setup

Broccoli hyperspectral images were collected with a HinaLea 4200 hyperspectral camera and converted to reflectance spectra. The camera covers the wavelengths ranging from 400nm to 1000nm with a resolution at 4nm (based on full width at half maximum), resulting in 300 wavebands. Halogen lamps were used as illuminators in an imaging chamber. Within the chamber, each broccoli sample was placed on a black plate with matte black siding to absorb redundant light in order to minimize scattering. Hyperspectral measurements of three biological replicates were carried out at every time point and the experiment was repeated three times.

Pre-processing Reflectance Spectra

Pre-processing of the measured spectra for noise and illumination variation was required prior to analysis. The measured reflectance spectra consistently contained higher levels of noise at the two ends of the wavelength range. In addition, since the illuminator used was a point light source and did not evenly cover the entire imaging surface. As a result, the center of the imaging plane was brighter than the outer edge. Fig. 1 (d) shows examples for the issues mentioned above. To mitigate these issues, first, a median filter of length 5 along the wavelength axis was applied to the reflectance spectra. Next, responses below 500 nm and above 900 nm were removed due to the high noise levels. Finally, in order to reduce the magnitude difference caused

by point light source, we applied l_2 normalization in which each spectral signature is normalized to have unit norm.

Segmenting Floret from Background

After pre-processing spectra, the regions of florets were segmented from the remainder of the hyperspectral cube. This segmentation was accomplished in two steps: (1) segmenting the broccoli sample from the black background; (2) segmenting the floret from the stalk. For the first stage, Fig. 1 (a) and (d)-(e) illustrates the spectral differences between the broccoli and the black background. Namely, the broccoli spectra have a bump around 550nm wavelength (visible bands of green) and a sharp increase around 700nm wavelength (Near infrared/Red edge whereas the spectra for the black background are nearly flat up to 800nm and then increases rapidly. Given these significant spectral differences, the k-means clustering algorithms was applied to cluster the pixel spectra into two groups, broccoli and background. After clustering, a morphological image closing operation was applied to connect any disconnected points. An example of the segmented results is shown in Fig. 1 (b).

Fig 1. RGB image and spectra. (a) Broccoli sample placed on a black plate. (b) Segmented broccoli sample. (c) Segmented broccoli floret. (d) Reflectance measured by HinaLea 4200 hyperspectral camera. (e) Preprocessed spectra. The color of spectra in the (d)-(e) is corresponding to the points in (a).

Since the glucosinolates concentration was measured on broccoli spores, we hypothesized that focusing on the spectra of broccoli flower will generate stronger correlation than analyzing the spectra of entire broccoli. In order to segment the floret from the stalk, we applied the GraphCut algorithm [18] of the image segmentation toolbox in Matlab 2019b [19]. The algorithm was seeded by the user providing a marking that denotes the broccoli flower and the background including broccoli pedicle. The segmentation took around 5 to 10 seconds for each image. The segmented results are shown in Fig. 1 (c).

Unmixing and correlation with glucosinolates information

The hyperspectral image collects a high-dimensional image cube that describes each pixel as the radiance or the reflectance at a range of wavelengths across the electromagnetic spectrum. The spectrum of a pixel is usually determined by the material of the object surface. With the assumption that the measured spectrum is consists of a set of constituent spectra, also known as endmembers, spectral unmixing is defined as decomposing the mixed spectrum into a collection of endmembers and their corresponding proportions, also known as abundances [20]. A well-known spectral model (and the most commonly applied to perform hyperspectral unmixing) is the linear mixing model (LMM) which represents each measured spectrum as a convex combination of endmembers as shown in Equation 1 [20],

$$s_i = \sum_{k=1}^{M} a_{ik} e_k + \varepsilon_i \text{ such that } \sum_{k=1}^{M} a_{ik} = 1, a_{ik} \in [0,1] \qquad (1)$$

where s_i is the spectrum of pixel i, ε_i is the noise vector, M is the number of endmembers, e_k is k^{th} endmember, and a_{ik} is the corresponding abundance value. The objective of each unmixing broccoli sample is to find a set of endmembers and abundances that can represent the freshness of broccoli. Thus, in this work, we attempt to estimate endmembers that represent the range of "freshness" levels in the samples. Then the associated abundances for the endmembers corresponding to "fresh" samples can use viewed as a freshness indicator for the sample. The endmembers and abundances were estimated using two approaches averaging (as described below in Section A) or the application of the SPICE algorithm (as described in Section B).

A. Unmixing with averaging spectra as endmembers

In the averaging approach, the endmembers were extracted by averaging the broccoli spectrum from two extreme storage conditions. Specifically, $\boldsymbol{e}_1$ is the average from broccoli on day 1, representing the best fresh level. $\boldsymbol{e}_2$ is the average from broccoli kept under room temperature for 12 days, representing the least fresh level. The greater a_{i1} indicates more fresh level of pixel *i* in the broccoli sample.

The abundance values were then estimated by optimizing the fully constrained least squares of each pixel with the above two endmembers as shown in Equation 2 [22].

$$\underset{a_{ik}}{\operatorname{argmin}} \sum_{i=1}^{N} |\boldsymbol{s}_i - \sum_{k=1}^{M} a_{ik}\boldsymbol{e}_k|^2 \; such\ that \; \sum_{k=1}^{M} a_{ik} = 1,\ a_{ik} \in [0,1] \quad (2)$$

where $M = 2$ in this case.

B. Unmixing with SPICE algorithm

Instead of extracting average spectra as endmembers, the sparsity promoting iterated constrained endmember (SPICE) algorithm benefits from simultaneous estimating the shape and number of endmembers as well as the abundances [21]. The algorithm is initialized with a large number of endmembers and iteratively updates the estimated endmembers and abundances by optimizing Equation 3 using an alternating optimization approach,

$$\underset{a_{ik},\, \boldsymbol{e}_k}{\operatorname{argmin}} \left[\frac{1-\mu}{N}\sum_{i=1}^{N} |\boldsymbol{s}_i - \sum_{k=1}^{M} a_{ik}\boldsymbol{e}_k|^2 + \mu V + SPT\right],\ SPT = \sum_{k=1}^{M} \frac{\Gamma}{\sum_{i=1}^{N} a_{ik}} \sum_{i=1}^{N} a_{ik} \quad (3)$$

where V is the sum of variances among estimated endmembers, μ is the regularization parameter to balance the reconstruction error and variance, $\boldsymbol{\Gamma}$ is a constant that decide the proportion values are driven to zero, and $\boldsymbol{a'}_{ik}$ is the abundance value for the ith pixel in the kth endmember from the previous iteration. After each iteration, endmembers which are not being used to represent the data are pruned from the overall endmember set[1].

C. Correlating abundance with glucosinolates concentration level

The estimated abundance vectors $\hat{\boldsymbol{a}} = \{\hat{a}_1, \hat{a}_2, ..., \hat{a}_k\} \in \mathbb{R}^{1\times M}$ for each broccoli sample (where the value $\hat{a}_k$ is the average abundance of all pixels over the region of interest as $\hat{a}_k = \frac{1}{N}\sum_{i=1}^{N} a_{ik}$, where N denotes the number of pixels) were used to attempt to predict measured glucosinolates concentration values. Specifically, a multi-variable linear regression (MLR) model as Equation

[1] The Matlab and Python implementation for SPICE can be found here: github.com/GatorSense

4 was fit using least squares estimation approaches to predict the glucosinolates concentration value,

$$glucosinolate \sim b + \sum_{k=1}^{M} w_k \hat{a}_k \quad (4)$$

where b is the bias, w_k is the coefficient for $\hat{a}_k$, M is the number of estimated endmembers.

Extraction of total glucosinolates for HPLC quantification

HPLC-UV analysis of total glucosinolates was extracted according to previously defined methods with some modifications [22]. Raw materials from previously harvested broccoli florets were stored at -80°C and further samples were taken out to be dispersed in liquid nitrogen. 100 mg of samples was weighed and crushed to fine powder using mortar and pestle. Subsequently, crushed tissue powder was dissolved in 1 ml of 50 % methanol contained in the 1.5 ml eppendorf tube. The tubes were further kept at 65°C for 1 hour in the water heating bath. Samples were then centrifuged at 15000 g for 10 minute. The supernatant was filtered through a 0.22um hydrophilic PTFE syringe filter (Sigma Aldrich, USA). HPLC analysis was done with the flow rate of 0.4 ml/min at a column temperature of 40°C with a wavelength of 227 nm. The solvent used were water and 100 % acetonitrile. The individual glucosinolates were estimated by their HPLC peak area with reference to a desulfo-sinigrin method [22]. Total peak area was calculated from broccoli florets from day 1, 3, 5, 7, 9, 11 when stored at growth chamber (25°C)

and cold temperature (4°C). Four biological replicate were used for each time point during the study.

RNA extraction and gene expression studies using Quantitative real-time PCR

Florets tissue samples from day 1, 3, 5 were chosen for glucosinolates pathway expression analysis. Total RNA was isolated from broccoli floret tissue stored in liquid nitrogen using TRIZOL (Ambion, life Technologies) method and DNase treatment (Turbo DNA free, Thermo-fisher). First strand cDNA synthesis with 1µg of total RNA was performed using reverse transcription kit (Applied Biosystems). For quantitative real-time RT-PCR, primers were designed using Primer Quest, Integrated DNA Technologies (IDT) software. The primers of glucosinolates pathway genes were listed in Table 1. Real time PCR reaction was performed in Applied Biosystems qPCR machine (Thermofisher). Total reaction was 10 µl for each gene in triplicates with thermocycler conditions as: 95°C for 10 min, 45 cycles for 95°C for 30 sec, 60°C for 30 sec. Relative gene expression was calculated by ΔCT method. Actin 2 was used as an internal control. This experiment was repeated twice.

Table 1 : List of primers for quantitative PCR performed for glucosinolates pathway in Broccoli

Glucosinolates biosynthetic genes	Sequence
BO_ACTIN2-FORWARD	TGGTCGTGACCTTACTGACTAT

BO_ACTIN2-REVERSE	TCACTTGTCCGTCGGGTAAT
BO_ST5B2-FORWARD	CCCATATACCCAACGGGTCG
BO_ST5B2-REVERSE	CCCATGAACTCAGCCAACCT
BO_MAM1-FORWARD	GGAATTATCCCTACCACCAGTTC
BO_MAM1-REVERSE	CAGAGGAGCAACATGAGATGAG
BO_CYP79F1-FORWARD	GTTAGGACAAGCGGAGAAAGA
BO_CYP79F1-REVERSE	CCATCAATGTTCCAACCTCTAAAC
BO_AOP2-FORWARD	GTGAGGAGTGATGTCCGTAAAG
BO_AOP2-REVERSE	GCCTCAACTGGTAACTCGAAA
BO_ESM1-FORWARD	CCGGAAGTAGCGTTGTTTACT
BO_ESM1-REVERSE	GTTAGGGTCGTCAAGGGATTT
BO_MAM3-FORWARD	ATCGTCCGTACAACAAGTCATC
BO_MAM3-REVERSE	GTATGTACTCTGGCCACCTTTC
BO_ESP-FORWARD	AGGACGATCGAGGCCTATAA
BO_ESP-REVERSE	GAATCCAGCTCCACCTCTTT
BO_FMOGSOX1-FORWARD	GGATTAATAGCGGCCAGAGAG
BO_FMOGSOX1-REVERSE	GCGGGTCGGATTCAGATTTA

Results

Use HSI as tool to detect postharvest senescence in broccoli

First, spectra were downsampled to 5,000 per segmented broccoli sample via k-means clustering to accelerate computing. Downsampling was applied to the two segmentation scenarios being considered: (1) entire broccoli, and (2) broccoli florets, respectively. Next, the entire dataset was split into training, validation and testing sets. To be more specific, 48 samples under 12 conditions (2 storage conditions over 6 time stages) were randomly divided into 4 folds, one for testing, and the other 3 for training and validation. Each fold contains 12 samples, 1 replication from each condition. The training and validation dataset were shuffled in every repetition.

In the first step, two endmembers were calculated by averaging spectra from the most and least fresh replication in the training folds. The glucosinolates concentration and derived abundance feature for all training replications were applied to fit the MLR model. The training process was repeated for 10 times over 3 folds. In each repetition, we tested the trained model on the testing fold, calculated the mean and standard deviation of the testing and training prediction error in Table 2. In addition, a model was selected according to the root means square error (RMSE) and R-squared value from training and validation folds and was applied to the testing fold to generate the result shown in Fig. 2.

Table 2. Comparison of glucosinolates prediction error from endmember abundances

		Average Spectra		SPICE	
		RMSE	**R2**	**RMSE**	**R2**
Entire	**Training&Validation**	48.12 ± 1.50	0.68 ± 0.02	44.93 ± 1.37	0.72 ± 0.02

Broccoli	**Testing**	28.81 ± 3.13	0.82 ± 0.04	26.14 ± 4.87	0.85 ± 0.06
Broccoli Florets	**Training&Validation**	47.36 ± 1.52	0.69 ± 0.02	44.78 ± 1.23	0.72 ± 0.02
	Testing	26.72 ± 1.82	0.85 ± 0.03	21.34 ± 3.26	0.90 ± 0.03

Fig 2. Predicted glucosinolates on testing fold. x-axis indicates the real glucosinolates concentration, y-axis indicates the prediction. Markers in various shape and color denotes prediction with different methods. Markers that closer to the "x = y" line indicates more accurate prediction.

Next, endmembers were estimated from training folds via SPICE. Since the estimated endmembers highly depends on the parameter Γ, a various range of Γ, starting from 10 to 150 with stepsize 10, were explored. We conducted 10 repetitions over 3 folds for 15 Γ values. Similar to the first stage, with the estimated endmembers, the abundance feature can be derived from the training folds to fit the MLR model. Fig. 3 (a-b), (f-g) shows greater prediction error on validation folds with a smaller Γ, which indicates over-fitting of the approach. Namely, Since Γ determines the proportion of estimated endmembers to be eliminated, a smaller Γ results in a greater number of endmembers and more parameters that need to be estimated (and provide opportunity for overfitting). Fig. 3 (c-d), (h-i) illustrate the tendency of over-fitting with increasing number of endmembers M. In addition, according to Fig. 3 (e), (j), $M = 3$ was determined for both segmentation, since it is the most number over 450 replications. We tested the trained MLR models with estimated endmembers on the test fold, generating the prediction errors shown in Table 2. A model was selected via the same criterion from repetitions and was applied to the same test fold as the first stage. The prediction results are shown in Fig. 2.

Fig 3. Exploration of SPICE parameters. (a-e) The training and validation error across various parameter setting for broccoli florets. (f-j) The training and validation error across various parameter setting for entire broccoli replicate.

The visualization of unmixing result is shown in Fig. 4, where (a-b) plot the estimated endmembers with average and SPICE on broccoli florets. Correspondingly, (c-d) visualize the estimated abundance map for testing samples in day 1, day 5, and day 12, and (e-f) plot the histogram of abundance value. The distribution of abundance and the number of pixels associated with each endmember is informative of freshness over days. In addition, the abundance map for the 3rd endmember in SPICE shows a relatively high concentration in day 5. It would be worth to explore whether the 3rd endmember can reveal a transition status during the progress of decay.

Fig 4. Estimated endmembers and unmixing results of testing samples in day 1, 5 and 12. (a-b) Estimated endmembers with average and SPICE on broccoli florets. (c-d) Visualization of estimated abundance map for testing samples in day 1, day 5, and day 12. (e-f) Histogram of abundance value.

Indo-glucosinolate peaks increased during the postharvest senescence

To access the possibility that the glucosinolates can be applied as senescence indicator, we performed HPLC analysis to measure the total glucosinolates concentration during the postharvest stored broccoli. In HPLC analysis, we monitored total peak area for indole-glucosinolates, the most widely distributed glucosinolates, at six time points during a 12-day of period for the broccoli florets stored at room temperature (25°C) and cold temperature (4°C). Four biological replicates were analyzed at each timepoint. We found that there is a linear increase in indo-glucosinlates concentration throughout a 12-day period in broccoli when stored at room temperature (Fig 5). However, this changes were not observed during the cold storage treatment in broccoli. Thus, there is a strong correlation observed between the indo-glucosinolates levels and progression of postharvest senescence in broccoli. This data suggested that indo-glucosinlates can potentially serve as an 'freshness indicator' to define a freshness signature.

Fig 5 . Quantification of the indo-glucosinolates peak area by HPLC. Graph displayed the changes in the indo-glucosinolates level in the broccoli florets on day 1, 3, 5, 7, 9, 11. Data represented means ± SE bars (n=4 for each day).

Glucosinolates transcriptional levels were increased during the postharvest senescence

To further validate this correlation and examine how the glucosinolates biosynthetic pathway is affected during the postharvest senescence process, we carried out quantitative gene expression of key genes in the glucosinolates biosynthetic pathway and observed that the

355 expression of all genes involved in glucosinolates biosynthetic pathway were up-regulated when
356 stored at room temperature. Mostly, all the key candidates' genes showed significant increase in
357 transcript expression on day 5 when the broccoli florets were stored at room temperature
358 however, the increase in glucosinolates profile during the postharvest day 5 was significant but
359 less drastic than the senescent conditions (Fig 6). This data showed that glucosinolates levels
360 increased rapidly in room temperature when stored at the room temperature. In case of pathway
361 intermediate methylthioalkylmalate synthases (MAM1 and MAM3), there was 4.3 fold and 11
362 fold significant increase in transcript levels from day 1 to day 3 and day 3 to day 5, respectively
363 at room temperature. However, in cold conditions, MAM1 levels were undetectable on day 3 but
364 increased on day 5 by 5.3 fold (Fig 6). This implied that MAM1 levels were increased in higher
365 proportions under room temperature condition. Similar patterns were observed for MAM3,
366 *epithiospecifier modifier 1* (*ESM1*), α-ketoglutarate-dependent dioxygenase (*AOP2*),
367 epithiospecifier protein (*ESP2*), CYP79ST5B2 as their transcripts were significantly higher from
368 day 0 to day 5. However, under cold conditions, the increase in flavin-monooxygenases
369 (FMOGSOX2) transcript levels from day 0 to day 5 was not significant. This observation
370 provided evidence that the gene expression changes in glucosinolates pathway were associated
371 with postharvest storage conditions. Transcript levels for all genes were significantly higher at
372 25°C indicating that the cold temperature was inhibited indo-glucosinolate production in
373 postharvest broccoli. Our results suggested that there is correlation between senescence and
374 indo-glucosinlates concentration in postharvest broccoli.
375
376 **Fig 6. A flowsheet of Indo-glucosinolates biosynthetic pathway displaying the transcript**
377 **levels on day 1, 3, 5 for key enzymatic intermediates catalyzing the biosynthetic pathway.**

All the key genes in glucosinolates biosynthetic pathway are highlighted in yellow. Red bars in the graph at each step shows the transcript level of specific candidate genes at 25°C on day 1, 3, 5 whereas blue bars show the expression level of the genes at 4°C on day 1, 3, 5. Expression of each gene was normalized using actin as an internal control. Data represents means ± SE bars (n=3). Asterisks (*) indicate statistically significant differences from day 1 (control) to day 3, day 5 (storage temperature conditions) ($p < 0.05$).

Outliers

The smaller prediction error for testing fold compared with training and validation folds in Table 2 can be explained by the observed outliers S1 Fig. showed the prediction performance of the training fold with SPICE on the broccoli florets. The marker size and color are related to their prediction error. Apparently, the three circled outliers generated greater prediction error compared with others. The S1 Table listed the glucosinolates concentration of 4 replications kept in room temperature over 6 time points. Three bold numbers are corresponding to the circled outliers in S1 Fig. In rep 1, the glucosinolates concentration was increasing along days, while in rep 2-4, the bold number showed "abnormal" performance. An additional experiment was conducted, where the outliers were moved to the testing fold. S2 Fig. and S2 Table showed the prediction performance and error on the additional testing fold.

S1 Table. The glucosinolates concentration under 25°C over days

	Rep1	**Rep2**	**Rep3**	**Rep4**

Day1	11.9544	11.9405	14.2901	21.099
Day3	53.858	31.6877	75.4149	25.0054
Day5	129.0532	113.1505	122.6086	122.941
Day8	135.2934	151.8804	**348.884**	**82.8482**
Day10	182.7224	**80.5022**	192.528	261.347
Day12	200.8352	269.094	215.7358	213.3986

S2 Table. Comparison of prediction error on additional testing fold

		Average spectra		SPICE	
		RMSE	**R2**	**RMSE**	**R2**
Entire Broccoli	**Training &Validation**	31.81 ± 0.64	0.82 ± 0.01	29.24 ± 1.89	0.85 ± 0.02
	Testing	65.84 ± 0.32	0.50 ± 0.01	61.81 ± 2.71	0.58 ± 0.05
Broccoli florest	**Training &Validation**	29.19 ± 0.36	0.85 ± 0.01	27.54 ± 0.42	0.86 ± 0.01
	Testing	66.22 ± 0.22	0.49 ± 0.01	62.47 ± 0.70	0.58 ± 0.01

Discussion

The above experiments were conducted on both the entire broccoli sample and the segmented broccoli florets. Fig. 4 and Table 2 compared the prediction performance and error. Overall, results depicted that the estimated abundances can indicate change in the glucosinolates

410 concentration values. The prediction error can be explained by the fact that the measurement of
411 hyperspectral data and glucosinolates concentration were conducted across different sample
412 scales. Namely, the abundance values are derived from imaging across the entire surface of one
413 side of a broccoli sample, whereas the glucosinolates value is measured using only one small
414 component of the broccoli tissue. The RMSE values show that unmixing with broccoli florets
415 only has slightly less error than when using the entire broccoli sample. In addition, SPICE
416 outperforms the simple averaging. However, when considering the computing and operation
417 complexity, averaging spectra is a more straightforward approach to estimate endmembers as
418 compared with SPICE and does not require parameter selection.

419 In summary, hyperspectral imaging holds promising strength in demonstrating state of art
420 performance in the area of crop sciences through the modulation of imaging with spectroscopy.
421 As shown in this effort, HSI has the potential to provide quantitative parameters in understanding
422 postharvest senescence.

423

424 Acknowledgements

425

426 We thank Dr. Diane Rowland for providing the HinaLea 4200 hyperspectral camera and
427 converted to reflectance spectra for supporting in sample imaging. We thank Dr. Ru Dai and Dr.
428 Jeongim Kim for the HPLC analysis and troubleshooting. This work was supported by UF Seed
429 Fund (#P0175583 to A.Z., T.L.).

430

431 References

1. Angelino D, Jeffery E. Glucosinolate hydrolysis and bioavailability of resulting isothiocyanates: Focus on glucoraphanin. Journal of Functional Foods. 2014 Mar ;7:67–76.
2. Coupe SA, Sinclair BK, Watson LM, Heyes JA, Eason JR. Identification of dehydration-responsive cysteine proteases during post-harvest senescence of broccoli florets. Journal of Experimental Botany. 2003 Mar 1;54(384):1045–56.
3. Karimi Y, Maftoonazad N, Ramaswamy HS, Prasher SO, Marcotte M. Application of Hyperspectral Technique for Color Classification Avocados Subjected to Different Treatments. Food Bioprocess Technol. 2012 Jan;5(1):252–64.
4. Shewfelt RL, Heaton EK, Batal KM. Nondestructive Color Measurement of Fresh Broccoli. J Food Science. 1984 Nov;49(6):1612–3.
5. Feng Y-Z, Sun D-W. 2012. Application of hyperspectral imaging in food safety inspection and control: a review. Crit Rev Food Sci Nutr 52:1039–58.
6. Gowen A, Odonnell C, Cullen P, Downey G, Frias J. Hyperspectral imaging – an emerging process analytical tool for food quality and safety control. Trends in Food Science & Technology. 2007 Dec;18(12):590–8.
7. Singh CB, Jayas DS, Paliwal J, White NDG. Fungal Damage Detection in Wheat Using Short-Wave Near-Infrared Hyperspectral and Digital Colour Imaging. International Journal of Food Properties. 2012 Jan;15(1):11–24.
8. Chen Y-R, Chao K, Kim MS. Machine vision technology for agricultural applications. Computers and Electronics in Agriculture. 2002 Nov;36(2–3):173–91.
9. Ariana DP, Lu R, Guyer DE. Near-infrared hyperspectral reflectance imaging for detection of bruises on pickling cucumbers. Computers and Electronics in Agriculture. 2006 Aug;53(1):60–70.
10. Cheng X, Chen YR, Tao Y, Wang CY, Kim MS, Lefcourt AM. 2004. A novel integrated PCA and FLD method on hyperspectral image feature extraction for cucumber chilling damage inspection. Trans ASAE 47:1313–20
11. Noh HK, Lu R. Hyperspectral laser-induced fluorescence imaging for assessing apple fruit quality. Postharvest Biology and Technology. 2007 Feb;43(2):193–201.
12. ElMasry G, Wang N, Vigneault C. 2009. Detecting chilling injury in Red Delicious apple using hyperspectral imaging and neural networks. Postharvest Biol Technol 52:1–8.
13. Li X, He Y. Non-destructive measurement of acidity of Chinese bayberry using Vis/NIRS techniques. Eur Food Res Technol. 2006 Oct;223(6):731–6.
14. Zhu Q, Huang M, Zhao X, Wang S. Wavelength Selection of Hyperspectral Scattering Image Using New Semi-supervised Affinity Propagation for Prediction of Firmness and Soluble Solid Content in Apples. Food Anal Methods. 2013 Feb;6(1):334–42
15. Cernadas RA, Benedetti CE. Role of auxin and gibberellin in citrus canker development and in the transcriptional control of cell-wall remodeling genes modulated by Xanthomonas axonopodis pv. citri. Plant Science. 2009 Sep;177(3):190–5.
16. Xing J, Guyer D, Ariana D, Lu R. Determining optimal wavebands using genetic algorithm for detection of internal insect infestation in tart cherry. Sens & Instrumen Food Qual. 2008 Sep;2(3):161–7.
17. Hernandez-Hierro JM, Esquerre C, Valverde J, Villacreces S, Reilly K, ´ Gaffney M,

476 Gonzalez-Miret ML, Heredia FJ, O'Donnell CP, Downey G. ´ 2014. Preliminary study
477 on the use of near infrared hyperspectral imaging for quantitation and localisation of total
478 glucosinolates in freeze-dried broccoli. J Food Eng 126:107–12.
479 18. Kwatra V, Schödl A, Essa I, Turk G, Bobick A. Graphcut textures: image and video
480 synthesis using graph cuts. ACM Transactions on Graphics (ToG). 2003 Jul 1;22(3):277-
481 86.
482 19. Gilat A. MATLAB: An introduction with applications. New York:: Wiley; 2008.
483 20. Keshava N, Mustard JF. Spectral unmixing. IEEE Signal Process Mag. 2002
484 Jan;19(1):44–57.
485 21. Zare A, Gader P. Sparsity Promoting Iterated Constrained Endmember Detection in
486 Hyperspectral Imagery. IEEE Geosci Remote Sensing Lett. 2007 Jul;4(3):446–50.
487 22. Lee JG, Lim S, Kim J, Lee EJ. The mechanism of deterioration of the glucosinolate-
488 myrosynase system in radish roots during cold storage after harvest. Food Chemistry.
489 2017 Oct;233:60–8.

490

491 Supporting information

492 **S1 Fig. Predicted glucosinolates on training folds.** x-axis indicates the real glucosinolates
493 concentration, y-axis indicates the prediction. Markers that closer to the "x = y" line indicates
494 more accurate prediction. The marker size and color is corresponding to the prediction error, the
495 bigger and brighter markers indicate greater error.

496

497 **S2 Fig. Predicted glucosinolates on additional testing fold**. x-axis indicates the real
498 glucosinolates concentration, y-axis indicates the prediction. Markers in various shape and color
499 denotes prediction with different methods. Markers that closer to the "x = y" line indicates more
500 accurate prediction.

501

502

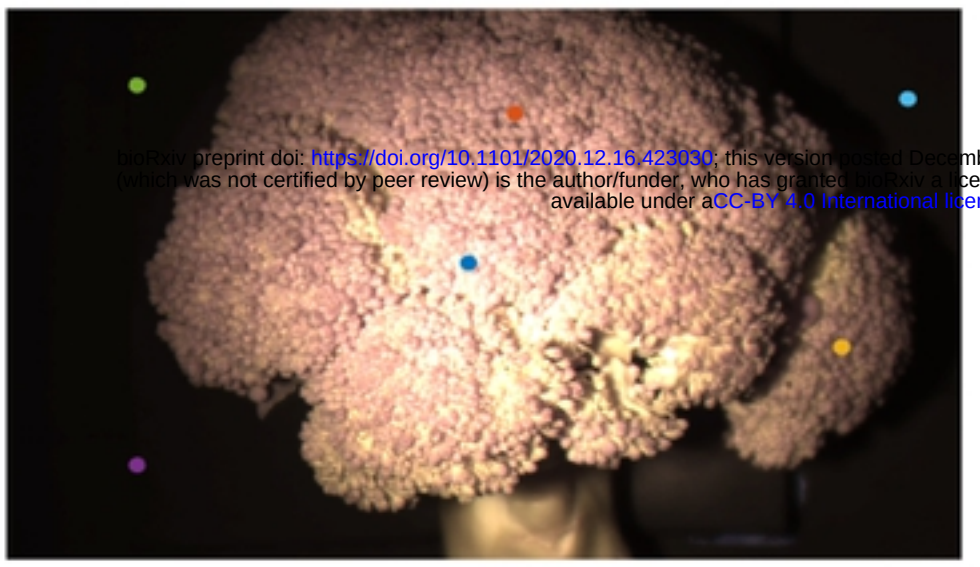

(a) RGB image of broccoli

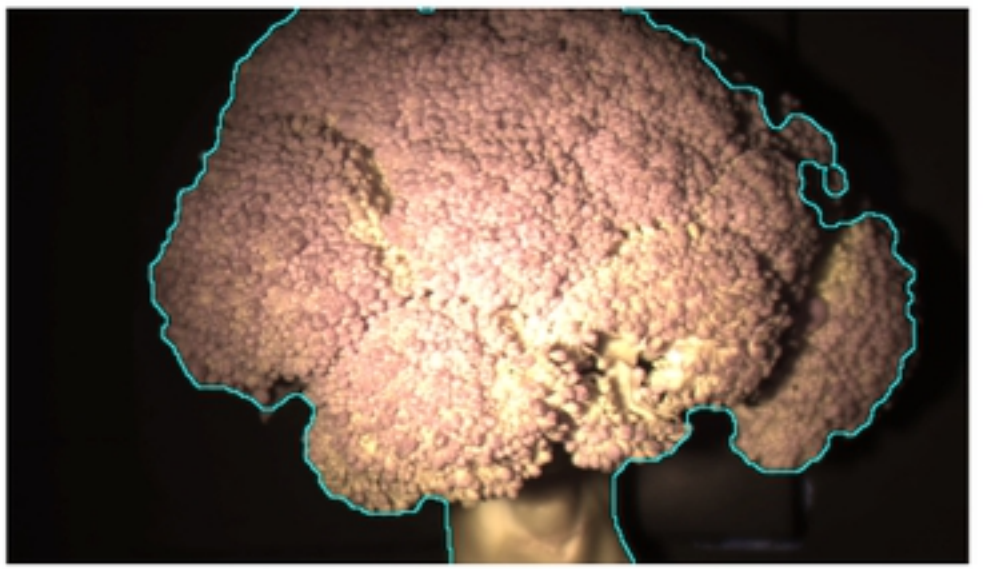

(b) Segmented broccoli

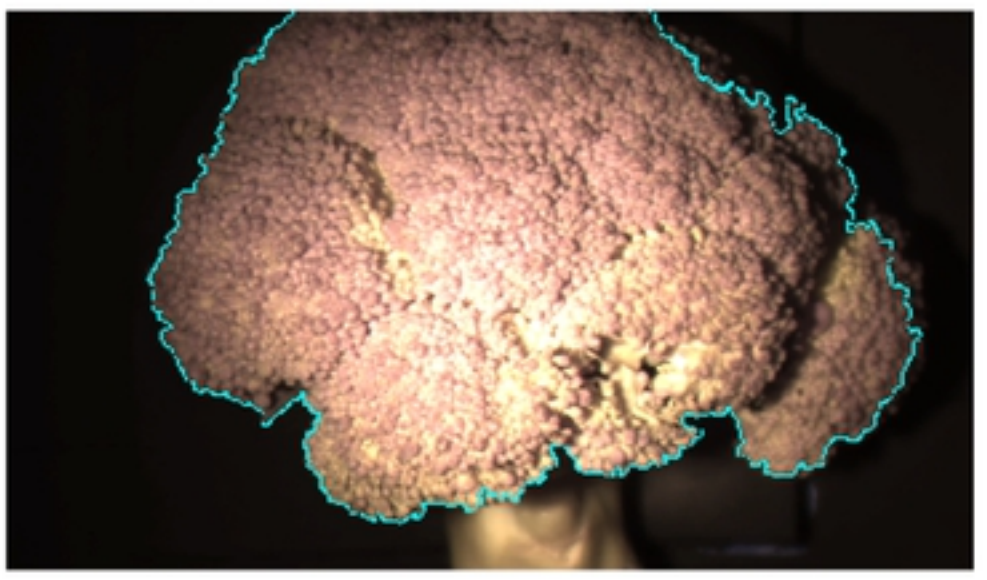

(c) Segmented broccoli flower

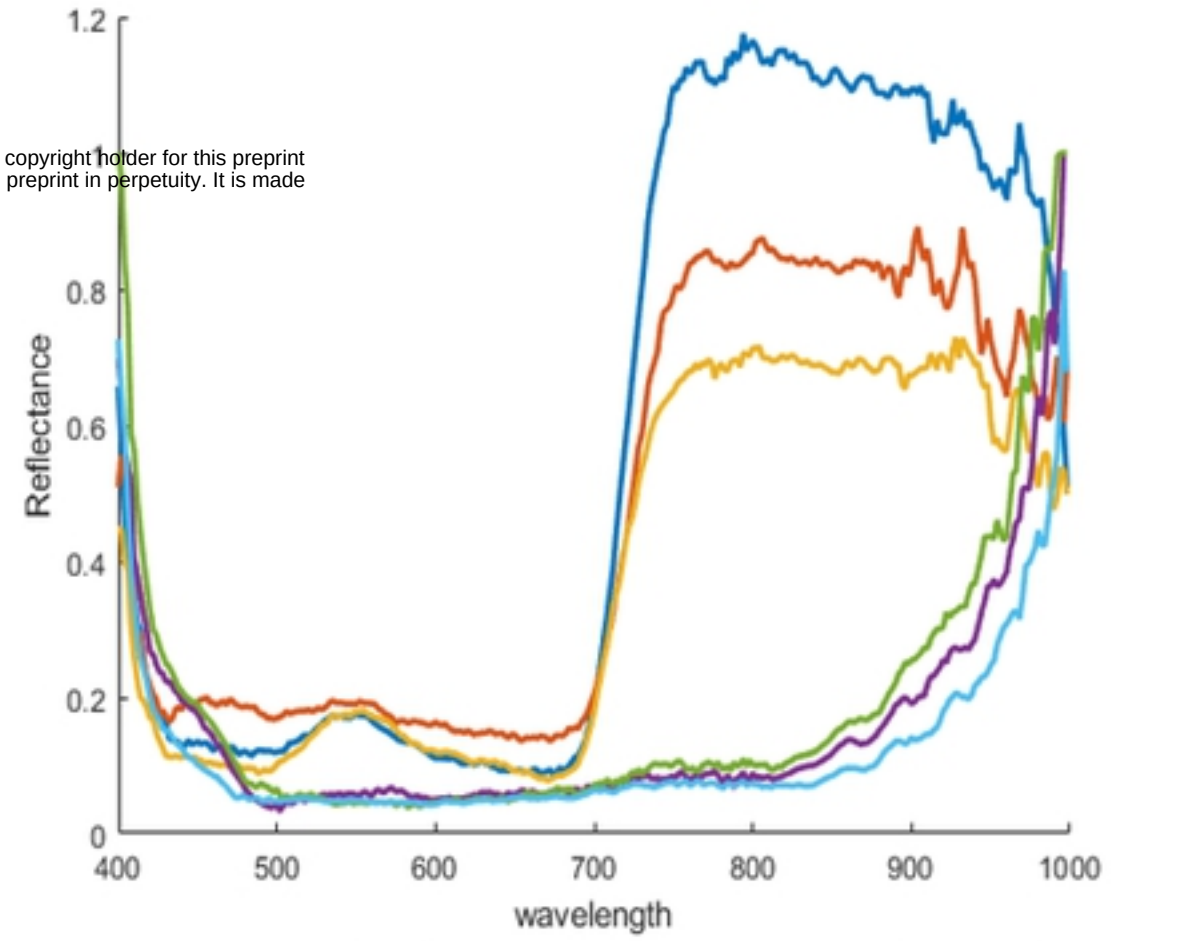

(d) Raw spectra of points

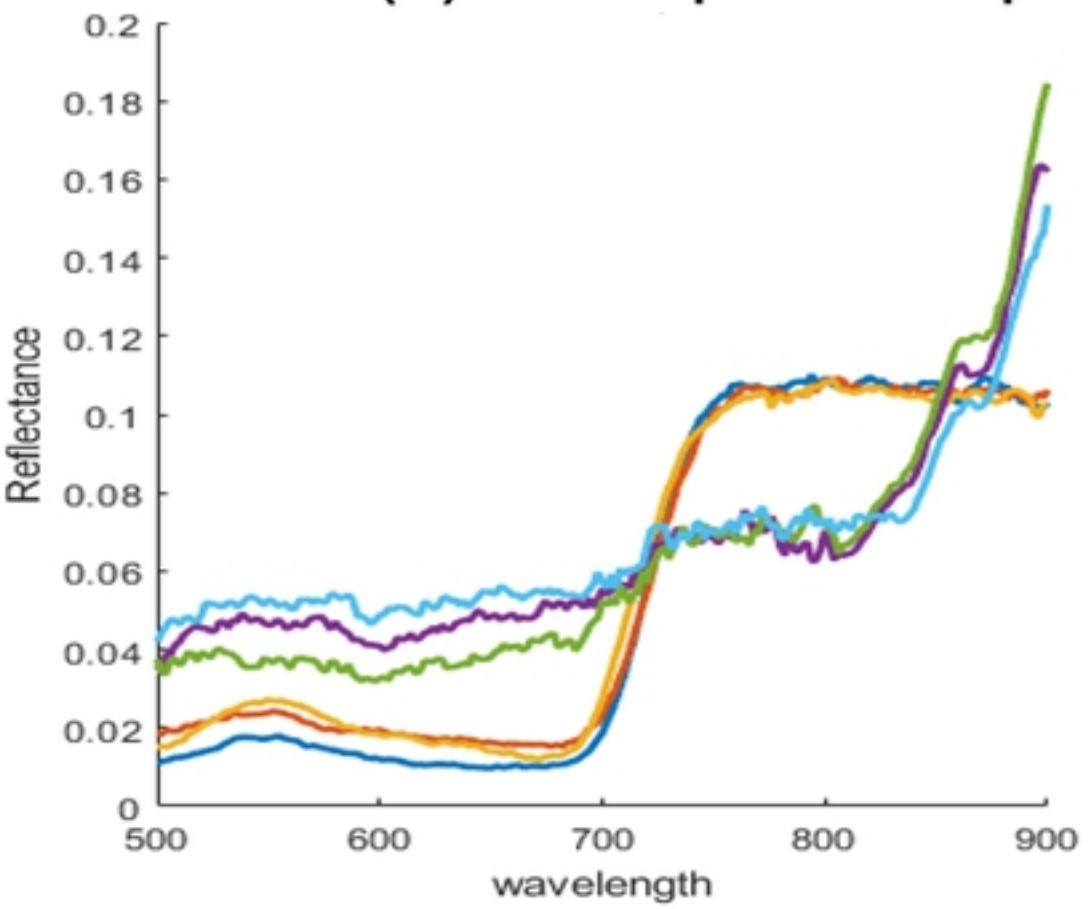

(e) Preprocessed spectra

Fig 1

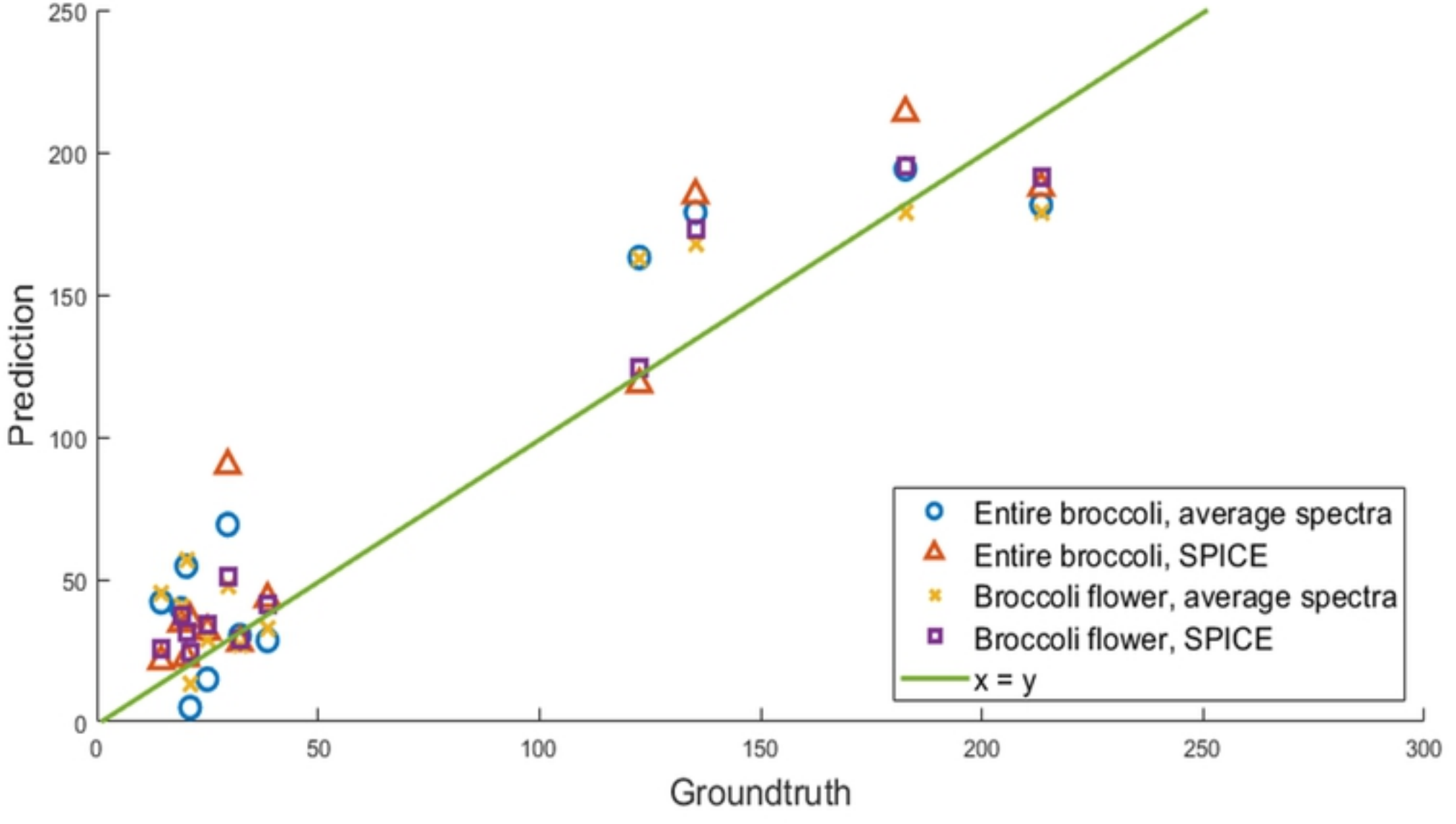
Prediction
Groundtruth
0
50
100
150
200
250
300
Entire broccoli, average spectra
Entire broccoli, SPICE
Broccoli flower, average spectra
Broccoli flower, SPICE
x = y

Fig 2

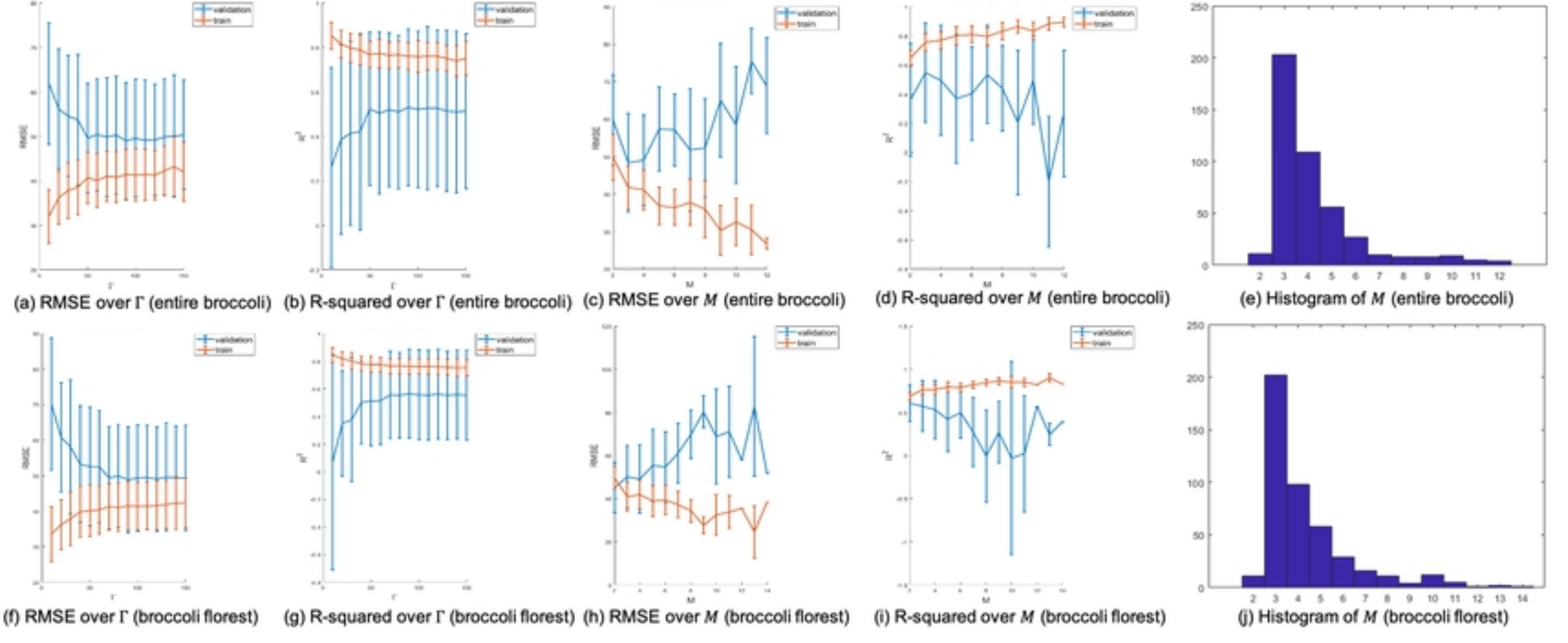

(a) RMSE over Γ (entire broccoli) (b) R-squared over Γ (entire broccoli) (c) RMSE over M (entire broccoli) (d) R-squared over M (entire broccoli) (e) Histogram of M (entire broccoli)

(f) RMSE over Γ (broccoli florest) (g) R-squared over Γ (broccoli florest) (h) RMSE over M (broccoli florest) (i) R-squared over M (broccoli florest) (j) Histogram of M (broccoli florest)

Fig 3

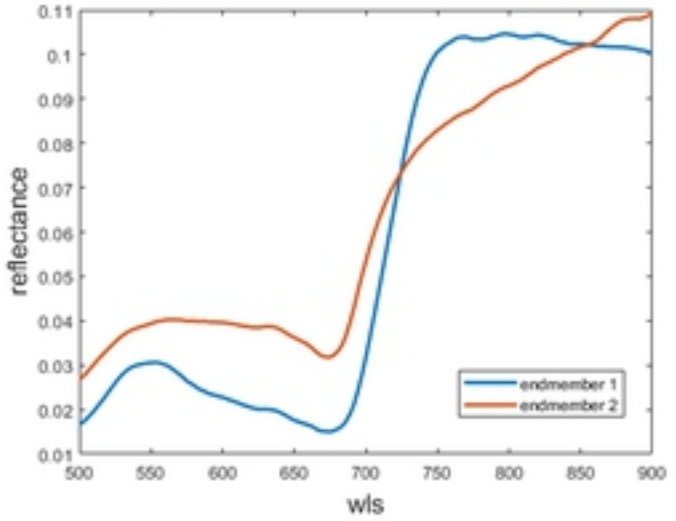

(a) Average spectra as endmembers

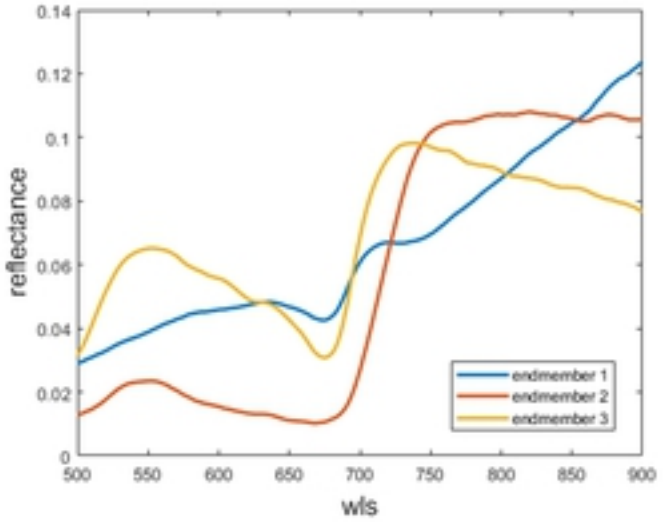

(b) Estimated endmembers by SPICE

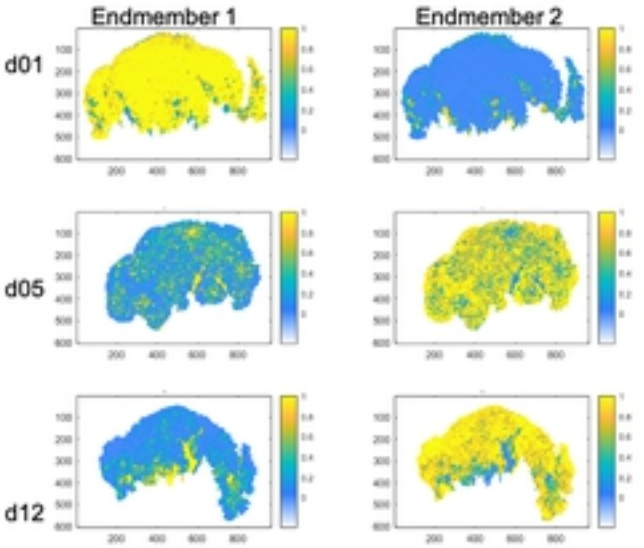

(c) Abundance map generated by average spectra

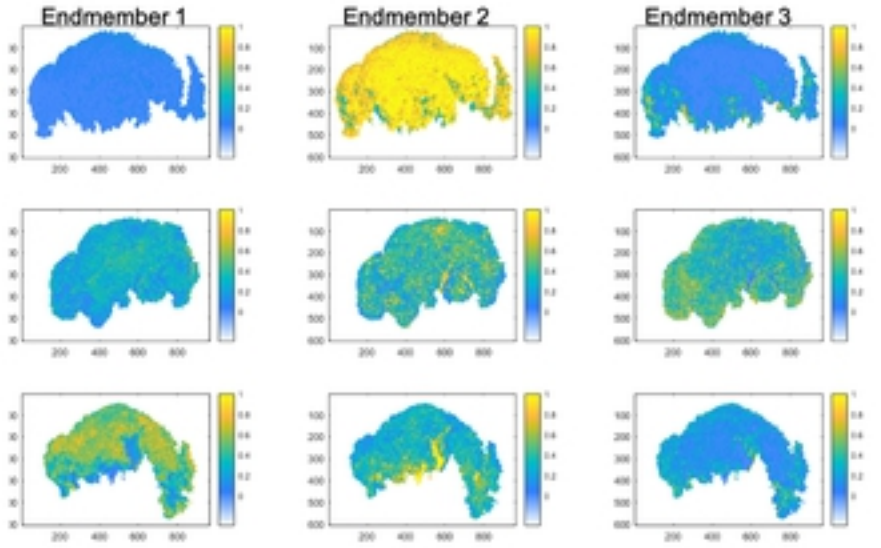

(d) Abundance map generated by SPICE

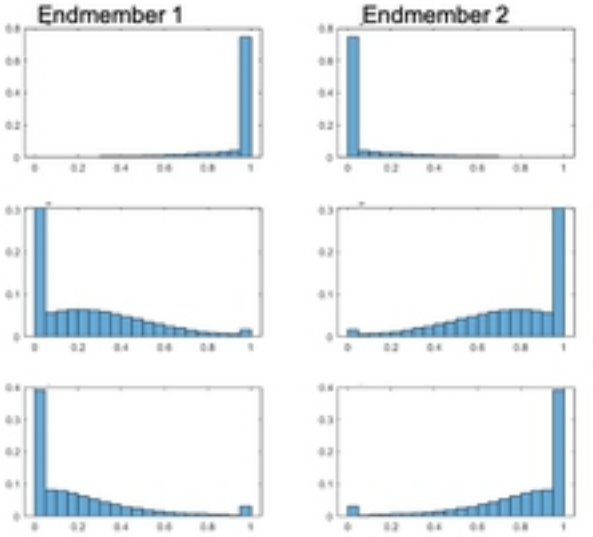

(e) Histogram of abundance value generated by average spectra

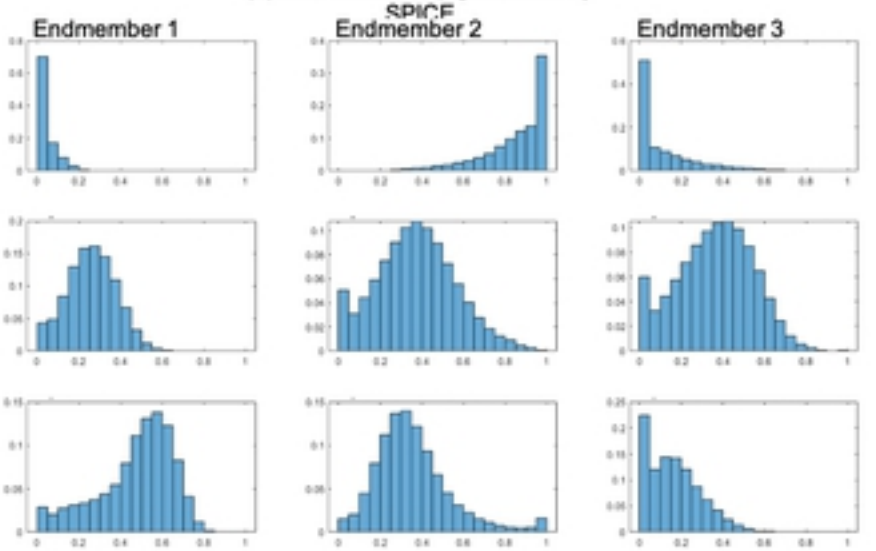

(f) Histogram of abundance value generated by SPICE

Fig 4

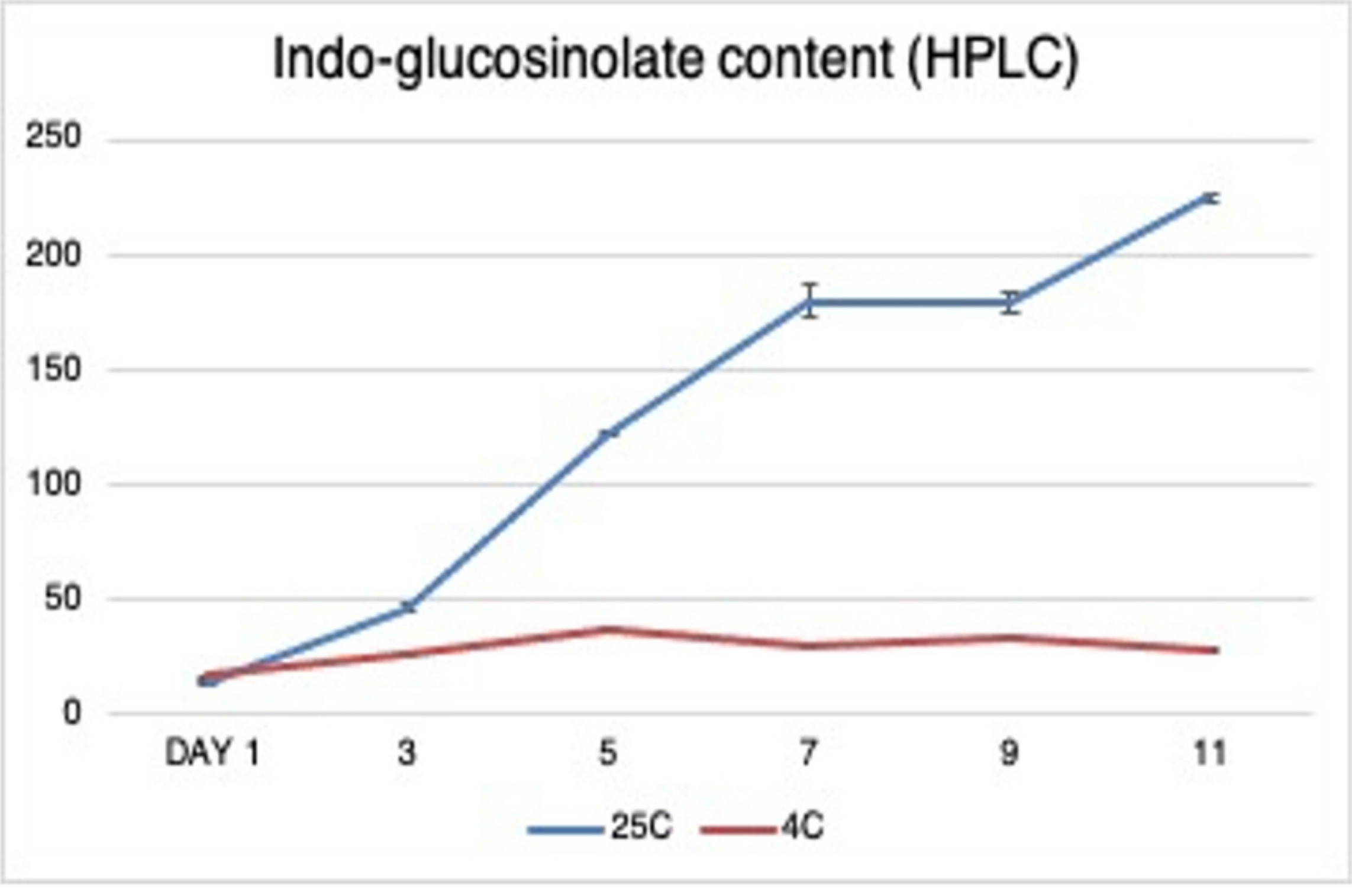
Indo-glucosinolate content (HPLC)
250
200
150
100
50
0
DAY 1
3
5
7
9
11
25C
4C

Fig 5

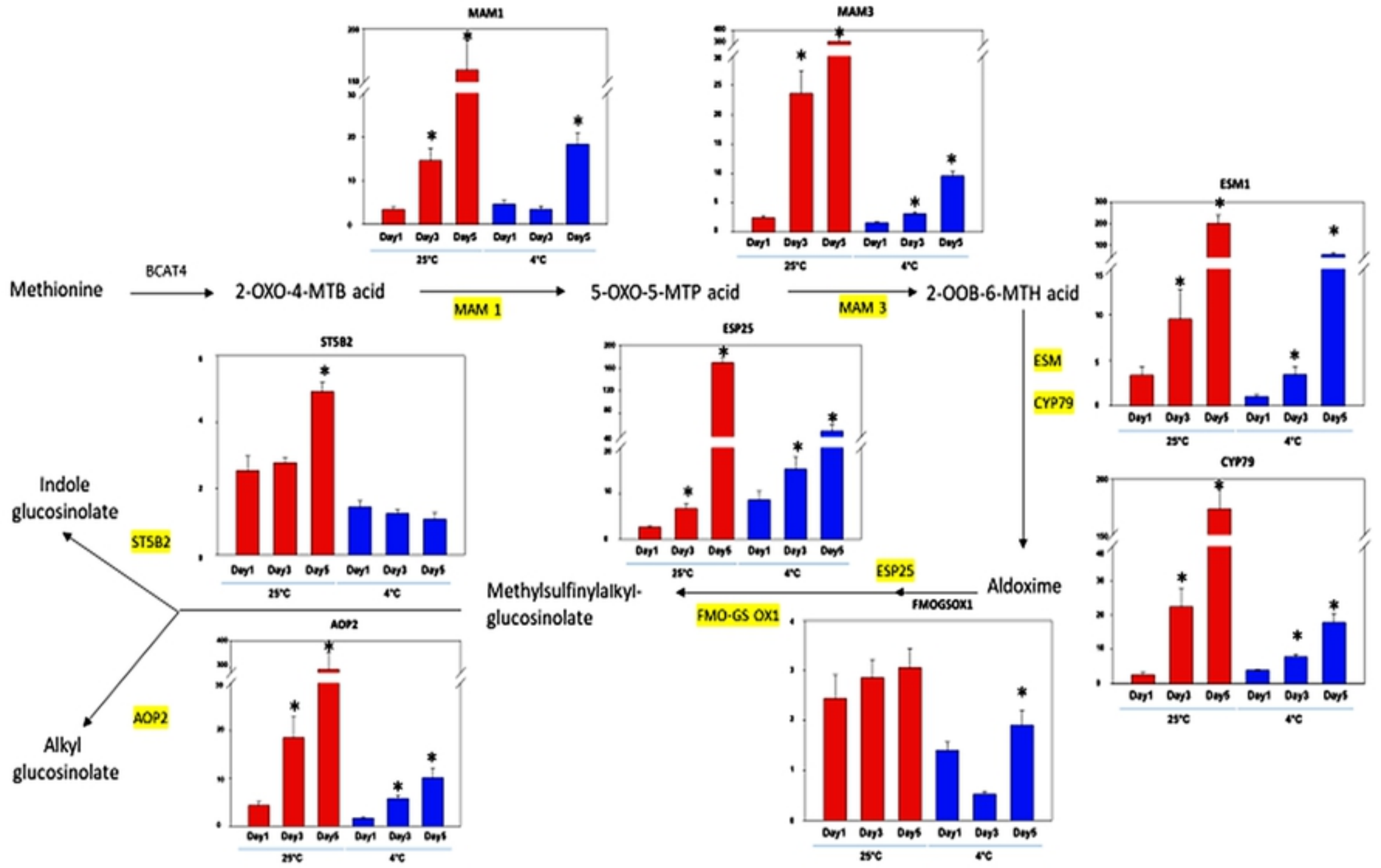
MAM1
MAM3
ESM1
CYP79
Methionine
BCAT4
2-OXO-4-MTB acid
MAM 1
5-OXO-5-MTP acid
MAM 3
2-OOB-6-MTH acid
ESM
CYP79
ESP25
ST5B2
Indole glucosinolate
ST5B2
Methylsulfinylalkyl-glucosinolate
ESP25
Aldoxime
FMO-GS OX1
FMOGSOX1
AOP2
AOP2
Alkyl glucosinolate
Day1
Day3
Day5
25°C
4°C

Fig 6